

J-PAS: A value-added catalogue of optical line intensities for nebular emission galaxies (JOLINES)

J.A. Fernández-Ontiveros^{1,2*}, C. López-Sanjuan^{1,2}, A. Hernán-Caballero^{1,2}, A. Lumbreras-Calle¹, J. Iglesias-Páramo³, A. Torralba⁴, R.M. González Delgado³, A. del Pino³, Rahna P.T.¹, I.E. López⁵, R. Amorín³, J.M. Vílchez³, C. Kehrig³, I. Breda⁶, D. Fernández Gil¹, F.D. Arizo-Borillo¹, A. Giménez-Alcázar³, E. Pérez-Montero³, F.J. Sáez Ruiz¹, N. Acharya¹, R. Abramo⁷, J. Alcaniz⁸, N. Benítez⁹, S. Bonoli^{10,1}, S. Carneiro⁸, J. Cenarro^{1,2}, D. Cristóbal-Hornillos¹, S. Daflon⁸, R. Dupke⁸, A. Ederoclite^{1,2}, C. Hernández-Monteagudo^{11,12}, J. Liu¹³, A. Marín-Franch^{1,2}, C. Mendes de Oliveira⁷, M. Moles¹, F. Roig⁸, L. Sodré Jr.⁷, K. Taylor¹⁴, J. Varela¹, H. Vázquez Ramió^{1,2}, and J. Zaragoza-Cardiel¹

¹ Centro de Estudios de Física del Cosmos de Aragón (CEFCA), Plaza San Juan 1, 44001 Teruel, Spain

² Unidad Asociada CEFCA-IAA, CEFCA, Unidad Asociada al CSIC por el IAA, Plaza San Juan 1, 44001 Teruel, Spain

³ Instituto de Astrofísica de Andalucía (IAA-CSIC), Glorieta de la Astronomía s/n, 18008 Granada, Spain

⁴ Institute of Science and Technology Austria (ISTA), Am Campus 1, A-3400 Klosterneuburg, Austria

⁵ INAF-Osservatorio di Astrofisica e Scienza dello Spazio di Bologna, via Gobetti 93/3, 40129, Bologna, Italy

⁶ Department of Astrophysics, University of Vienna, Türkenschanzstraße 17, 1180 Vienna, Austria

⁷ Departamento de Astronomia, Instituto de Astronomia, Geofísica e Ciências Atmosféricas, Universidade de São Paulo, São Paulo, Brazil

⁸ Observatório Nacional, Rua General José Cristino, 77, São Cristóvão, 20921-400, Rio de Janeiro, RJ, Brazil

⁹ Independent Researcher

¹⁰ Donostia International Physics Center (DIPC), Manuel Lardizabal Ibilbidea, 4, San Sebastián, Spain

¹¹ Instituto de Astrofísica de Canarias, C/ Vía Láctea, s/n, E-38205, La Laguna, Tenerife, Spain

¹² Universidad de La Laguna, Avda Francisco Sánchez, E-38206, San Cristóbal de La Laguna, Tenerife, Spain

¹³ National Astronomical Observatory of China, Chinese Academy of Sciences, Beijing, China

¹⁴ Instruments4, 4121 Pembury Place, La Canada Flintridge, CA 91011, U.S.A.

December 1, 2025

ABSTRACT

Emission lines in galaxy spectra provide unique information on the physical conditions of the interstellar medium, enabling the measurement of fundamental properties such as star formation rate, gas excitation, metallicity, or active galactic nucleus (AGN) activity. In this study, we present the value-added catalogue JOLINES (J-PAS optical line intensities for nebular emission galaxies), which provides emission-line fluxes in galaxies at from the spectrophotometric catalogues of miniJPAS, J-NEP and the J-PAS early data release (EDR). This catalogue will be updated with future data releases, offering a growing resource for the study of emission-line galaxies. To obtain reliable emission-line fluxes from narrow-band photometry, we employed spectral energy distribution (SED) fitting using CIGALE, a robust tool that reconstructs the continuum emission and ensures accurate flux measurements. This method effectively mitigates uncertainties associated with direct continuum subtraction techniques, and systematics such as absorption components in the emission lines. We validate our approach using simulated observations of galaxy spectra with added noise, testing the method's performance across different equivalent width (EW) regimes and emission-line strengths. Additionally, we compare the recovered emission-line fluxes with spectroscopic measurements from the Sloan Digital Sky Survey (SDSS) and the Dark Energy Spectroscopic Instrument (DESI). Our results show a tight correlation between photometric and spectroscopic fluxes, particularly for bright emission lines, with a typical dispersion of ~ 0.3 dex. Reliable fluxes are obtained for emission lines with $EW \gtrsim 20$ Å, in agreement with previous empirical studies. The current catalogue comprises approximately 13 900 sources with reliable flux measurements in the $H\alpha + [N II]$ complex and 7 200 in $[O III]\lambda 5007$, ensuring statistically robust samples for the brightest optical emission lines. This resource will be expanded in future J-PAS releases, facilitating large-scale studies of star formation, AGN activity, and galaxy evolution.

Key words. Catalogs – Surveys – Galaxies: active – Galaxies: evolution – Galaxies: star formation – Techniques: imaging spectroscopy

1. Introduction

The emission lines detected in galaxy spectra provide unique information on the physical properties of the interstellar medium (ISM) and allow us to measure fundamental properties for studying galaxy evolution, such as star formation rate (SFR), extinc-

tion, nebular gas excitation, and AGN fraction (Kewley et al. 2019). Accurate emission-line flux measurements are essential, as they directly trace the physical and chemical conditions in galaxies (Osterbrock & Ferland 2006) and reveal key processes such as star formation and AGN activity.

To reliably measure emission-line fluxes from narrow-band filters, it is crucial to have an accurate determination of the adjacent continuum emission. A poor assignment of the continuum

* e-mail: j.a.fernandez.ontiveros@gmail.com, jafernandez@cefca.es

can significantly affect the measurement of the emission-line flux. Direct subtraction of the continuum emission measured from one or a few filters adjacent to the one containing the emission line is a straightforward method, requiring only a limited number of additional observations. This technique is fast and provides a simple way to estimate line fluxes, particularly when the emission line is strong (e.g. Ly et al. 2007; Cook et al. 2019; Salzer et al. 2023; see Iglesias-Páramo et al. 2022 for extreme-emission-line galaxies in miniJPAS, where a larger number of continuum filters can be used). However, as the line flux decreases, errors in the determination of the adjacent continuum become more significant, necessitating the use of more sophisticated methods.

Machine learning techniques have been proposed as an alternative, where spectroscopic observations or synthetic models are used to train algorithms to predict the continuum and measure emission or absorption line fluxes in galaxy spectra (Ucci et al. 2018; Rhea et al. 2021; Dawson et al. 2021; Jalan et al. 2024) and in photospectra from narrow-band photometry (Martínez-Solaesche et al. 2021). The advantage of these techniques is their ability to measure emission lines with very low equivalent widths (EWs), down to just a few angstroms, and separate emission-line blends (e.g. $H\alpha + [N II]\lambda 6548, 6583$) based on the properties of the galaxy training sample (Martínez-Solaesche et al. 2022). However, these methods carry a risk: the trained network may propagate biases from the training dataset by overfitting results derived from low signal-to-noise (S/N) data, requiring careful monitoring and control (Leung & Bovy 2019; Dhar & Shamir 2022; Huertas-Company & Lanusse 2023).

Another commonly used method is spectral energy distribution (SED) fitting, which reconstructs the continuum by fitting models to the galaxy multi-band spectrum (e.g. Lee et al. 2012; Nakajima et al. 2012). Although SED fitting has the disadvantage of being influenced by the models used to approximate the continuum, this issue can be mitigated by employing diverse model libraries. By exploring a wide parameter space, SED fitting ensures robust continuum reconstruction and minimises the introduction of artificial features, which are easier to identify and avoid compared to machine-learning methods. Additionally, restricting the use of models that could add unwanted features in the continuum further improves its reliability. In particular, the large number of filters and the wide wavelength coverage of J-PAS surveys offer excellent opportunities for applying SED fitting techniques (Mejía-Narváez et al. 2017; González Delgado et al. 2021). The reliability of this method has been demonstrated by Vilella-Rojo et al. (2015), Logroño-García et al. (2019), Lumbrales-Calle et al. (2022), Breda et al. (2024) and Rahna et al. (2025), by comparing spectroscopic fluxes from SDSS with emission-line fluxes measured from narrow-band photometry in J-PLUS (Cenarro et al. 2019) and miniJPAS (Bonoli et al. 2021).

In this work we present a catalogue of emission-line fluxes for galaxies in J-PAS, JOLINES (J-PAS Optical Line Intensities for Nebular Emission galaxies). The line fluxes are based on spectrophotometric data extracted from the precursors of the Javalambre-Physics of the Accelerated universe Astrophysical Survey (J-PAS; Benítez et al. 2014), i.e. miniJPAS and J-NEP (Hernán-Caballero et al. 2023), and the J-PAS early data release (EDR; Vázquez Ramió et al. in prep.). J-PAS is an unprecedented photometric sky survey of 8500 deg², conducted from the Javalambre observatory in Teruel (Spain), using a set of 57 narrow- and several SDSS broad-band filters. Throughout this study, we adopted a flat- Λ CDM cosmology with $H_0 = 73 \text{ km s}^{-1} \text{ Mpc}^{-1}$ and $\Omega_m = 0.27, \Omega_\Lambda = 0.73$. In Section 2, we explain the data obtained from J-PAS surveys. Section 3 describes the methodology for continuum fitting and emission-line

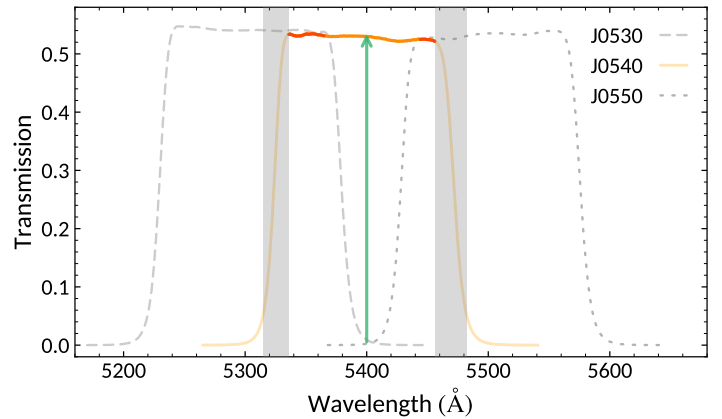


Fig. 1. Transmission profile of three J-PAS filters: J0530 (dashed grey line), J0540 (solid yellow line), and J0550 (dotted grey line). A flux measurement for a certain emission line (green arrow) from Table 1 is provided when the observed wavelength falls on the top 5% maximum transmission of the square filters (orange and red solid line), whereas filters with lines falling at the transmission profile wings ($> 5\%$; shaded grey area) are flagged as contaminated and discarded for the continuum fitting. Note that those cases will have a measurement in one of the adjacent filters, which always overlap at the maximum transmission (in red).

flux measurements. In Section 5, we present the comparison with measured line fluxes for objects with available spectroscopic observations. Finally, in Section 6, we summarise the results and discuss their implications for future studies.

Table 1. Optical bright emission lines considered to provide measurements derived from narrow-band photometry.

Name	Wavelength (Å)
[O II] λ 3727	3726.0, 3728.8
[Ne III] λ 3869	3868.8
H γ + [O III] λ 4363	4340.5, 4363.2
H β	4861.3
[O III] λ 4959	4958.9
[O III] λ 5007	5006.8
[O I] λ 6300	6300.3
[N II] λ 6548	6548.1
H α	6562.8
[N II] λ 6583	6583.5
[S II] λ 6724	6716.4, 6730.8
[S III] λ 9069	9068.6
[S III] λ 9531	9531.1

2. Observations and methods

The sample of galaxies in JOLINES was drawn from a query to the miniJPAS, J-NEP, and EDR dual catalogues¹ by selecting targets with a low probability of being star-like (i.e. stars or quasars; CLASS_STAR < 0.1) and with no flags in their photometric measurements (i.e. all FLAGS and MASK_FLAGS set to 0). An additional cut was applied to select sources with i -band magnitudes brighter than 21 mag, in order to exclude objects with very low S/N in the continuum determinations, and with photo- $z < 0.4$, to ensure that the H α line remains within the rest-frame spectral range. To derive emission-line fluxes from the photo-

¹ r -band detection in miniJPAS and J-NEP, i -band detection in EDR.

Table 2. Parameters and their respective sampling ranges for the various modules used in CIGALE v2025.0 SED fitting.

Parameters	Sampling range
<i>Star formation history: delayed model</i>	
Age of the main population	5, 8, 10, 13 Gyr
e-folding time	1, 5 Gyr
Age of the young burst	1, 5, 10, 100, 500 Myr
e-folding time young burst	5, 50, 100 Myr
Burst stellar mass fraction	0.0, 0.2, 0.4, 0.6, 0.8, 0.99
<i>Simple Stellar population: Charlot & Bruzual (2019)</i>	
Initial Mass Function	Chabrier (2003)
Metallicity	0.004, 0.01, 0.02, 0.03
Upper IMF limit	100 M _⊙
<i>Nebular emission</i>	
Ionisation parameter (log U)	-2.0, -3.0, -4.0
Gas metallicity (Z _{gas})	0.004, 0.011, 0.020, 0.033
Electron density (n _e)	100 cm ⁻³
<i>Dust extinction</i>	
Dust attenuation law	modified Charlot & Fall (2000)
ISM V-band attenuation (A_V^{ISM})	0.0, 0.2, 0.4, 0.6, 0.8, 1.0, 1.5, 2.0, 2.5, 3.0
Ratio of ISM to total attenuation ($\mu = \frac{A_V^{\text{ISM}}}{A_V^{\text{ISM}} + A_V^{\text{BC}}}$)	0.44
Power law slope of ISM attenuation	-0.7
Power law slope of birth clouds attenuation	-1.3
Number of models per redshift	345 600

metric measurements, we performed SED fitting with CIGALE² (Code Investigating GALaxy Emission; Boquien et al. 2019), owing to its versatility and efficiency in computing best-fits for large galaxy samples.

2.1. Flux catalogues and photo-zs

Fluxes from the miniJPAS, J-NEP, and EDR catalogues were extracted from the FLUX_APER_COR_3_0 column in the dual catalogue, which represents photometric fluxes measured within a three arcsecond aperture and corrected for aperture effects for sources detected in the *r* (miniJPAS and J-NEP) or the *i* bands (EDR). The aperture correction assumes point-like sources in the dual catalogue, ensuring consistent flux measurements despite challenges in extended sources like galaxies. We selected the APER_COR_3_0 aperture specifically to ensure robust spectrophotometric calibration across the full filter set. While this fixed aperture may not capture the total flux of extended sources, it is essential for minimising systematic scatter among continuum filters caused by varying observing conditions, such as changes in seeing and background depth (Vázquez Ramió et al. in prep.). To address potential flux losses in extended sources, the photospectrum of each galaxy was scaled by the factor required to match the *r*-band flux in FLUX_APER_COR_3_0 with that in FLUX_AUTO measurements. Photometric redshifts for individual sources are available in all catalogues and were calculated using the method described by Hernán-Caballero et al. (2021). This approach employs a customised version of LEPHARE (Arnouts & Ilbert 2011), optimised for J-PAS observations with a selection of 50 synthetic galaxy templates from

CIGALE to enhance photo-z accuracy for a subsample of galaxies. Additionally, a “galaxy locus recalibration” was performed, which adjusts systematic photometric offsets via median galaxy colours (Hernán-Caballero et al. 2023). Finally, redshift probability distributions were combined through conflation³, leveraging the precision of miniJPAS narrow-band filters and the depth of broad-band imaging from the Hyper-SuprimeCam Subaru Strategic Program (Hernán-Caballero et al. 2024). This integration improved the miniJPAS photo-z estimates, particularly for faint sources. Overall, the majority of sources in miniJPAS, J-NEP, and EDR catalogues with *i* < 21.5 mag have photo-z uncertainties of $|\Delta z| < 0.3\%$ (Hernán-Caballero et al. 2023, 2024).

The selection of emission-line filters was a key step in our methodology. We identified filters whose transmission profiles may include bright emission lines (see Table 1). Figure 1 illustrates the transmission profiles of three J-PAS narrow-band filters, represented as dashed, solid, and dotted lines. A filter is considered to contain an emission line when the observed wavelength of the line falls within the maximum transmission in the filter’s square profile. For instance, the maximum transmission region of the J0540 filter is highlighted in orange in Fig. 1, while the transmission wings are shown in yellow. A flux measurement is provided for a certain emission line (green arrow) when the observed line wavelength falls within this flat maximum transmission region. Conversely, potential contamination from nearby emission lines can occur when a transition falls within the filter’s transmission wings, due to uncertainties in the contribution of the line to the integrated flux. Thus, measurements affected by

² <https://cigale.lam.fr>

³ Conflation refers to the normalised product of independent probability density functions of the same underlying variable. This operation produces a combined estimate with reduced uncertainty.

potential contamination in the transmission wings, at transmission levels exceeding 5% (shaded grey area in Fig. 1), are flagged and excluded from the continuum fitting. Nevertheless, a flux measurement in those cases will be provided by adjacent filters, which always overlap at the maximum transmission (red solid line). We considered a filter as suitable continuum for SED fitting only if it contained no bright emission lines within either the maximum transmission region or the transmission wings.

Emission lines falling within ~ 150 Å in observed wavelength – comparable to the typical width of the J-PAS narrow-band filters – may be blended depending on the galaxy redshift. This situation frequently arises for pairs such as H β and [O III] λ 4959, the [O III] λ 4959, 5007 doublet, or H α and the [N II] λ 6548, 6583 doublet. In these cases, the JOLINES catalogue provides the total blended flux, and individual line intensities are recovered when possible using flux measurements from adjacent overlapping filters and the theoretical nebular ratios for the [O III] and [N II] doublets (see discussion in Sections 3.2 and 3.3). Conversely, doublets with small wavelength separations, such as [O II] λ 3726, 3729 and [S II] λ 6716, 6731, cannot be deblended in most cases, since their intrinsic ratios depend strongly on electron density and cannot be disentangled on theoretical grounds.

2.2. Continuum subtraction

For each galaxy, the continuum emission was estimated by fitting the photospectrum after masking the filters containing the bright emission lines listed in Table 1. CIGALE v2025.0 was chosen for the SED fitting procedure due to its efficiency in processing large samples of galaxies and its capability to provide Bayesian fitting estimates. Initially, spectrophotometric fluxes from the J-PAS catalogues were converted to mJy and transformed to the CIGALE input table format. Filter transmission profiles for J-PAS filters are available at the Spanish Virtual Observatory (SVO) service⁴ (Rodrigo et al. 2012; Rodrigo & Solano 2020). Since the main goal of the SED fitting process is to perform an accurate determination of the continuum level, we only take into account continuum-dominated filters to avoid possible biases in the best-fit continuum. These could be caused, for example, by the presence of very bright emission lines that may bias the best-fit solutions towards bluer continua, required to reproduce the line properties. On the other hand, the nebular continuum was taken into account for the fitting, since this component may contribute significantly to the optical/UV range in low-mass star-forming galaxies (e.g. Reines et al. 2010; Cardoso et al. 2022; Lumbrales-Calle et al. 2022) and radiogalaxies with strong emission lines (Dickson et al. 1995; Solórzano-Iñarra et al. 2004; Holt et al. 2007). The parameters of the nebular module in CIGALE were restricted to a relatively narrow grid, with three ionisation parameter values, four gas metallicities, and a single electron density of 100 cm^{-3} . This choice was motivated by the fact that emission lines are not included in the fitting process, so a compact parameter grid was adopted to reduce the computation time required for the main model library. Line flux uncertainties are derived from the quadratic propagation of the uncertainties associated with the photometric measurements and the best-fit continuum estimate.

To accommodate a wide diversity of galaxy properties in the continuum subtraction process, we used models encompassing a broad range of parameters, including stellar ages, star formation rates (SFRs), star formation histories, dust extinction, and metallicity. Table 2 shows a summary of the fitting modules adopted for CIGALE, the most relevant parameters, and their respective

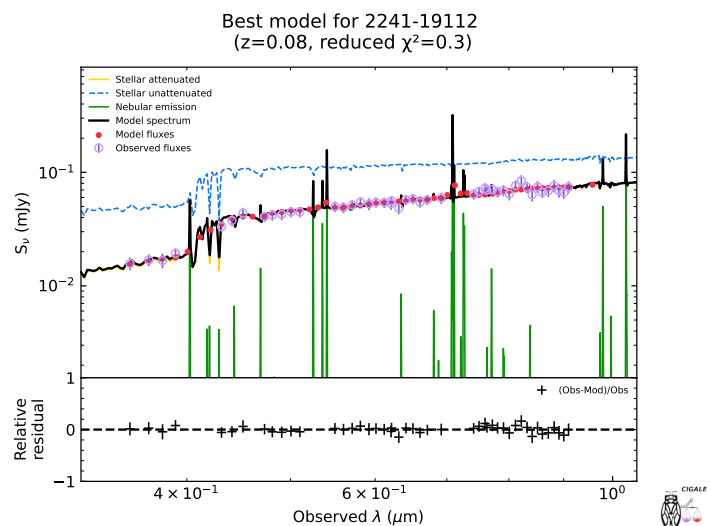


Fig. 2. Best-fit SED obtained with CIGALE for the miniJPAS galaxy 2241–19112. The upper panel displays the observed fluxes (purple circles), the best-fit fluxes derived from the fitting (red dots), the stellar continuum before (dashed blue line) and after (solid yellow line) applying dust attenuation, the nebular line plus continuum emission (solid green line), and the total model (solid black line). The lower panel presents the relative differences between the observed and modelled fluxes.

sampling ranges. This comprehensive grid, comprising approximately ~ 14 million models (345 600 per redshift in ~ 40 redshift bins between $z = 0$ and 0.4), enabled accurate reproduction of the continuum emission in J-PAS galaxies.

Figure 2 shows an example of the best-fit model obtained for the miniJPAS galaxy TILE-ID-NUMBER = 2241–19112. In this example, the best-fit attenuated stellar emission provides a robust description of the continuum, allowing us to subtract this component from the observed photospectrum. This is shown in more detail in Fig. 3 (left panel), where the modelled continuum (in dark grey), accounts for the absorption lines due to the old stellar populations, allowing us to correct the line fluxes measured in the narrow-bands (colourful dots). Bright emission lines of [O II] λ 3727, H β + [O III] λ 4959, [O III] λ 5007, and H α + [N II] λ 6548 stand out in the continuum-subtracted photospectrum shown in Fig. 2 (right panel). The scatter in the continuum fluxes (dotted black lines) is mainly caused by differences in the observing conditions, since all filters are acquired on different nights, typically over a period of a few months. Figure 3 shows how continuum subtraction using only line-adjacent filters could limit our measurements to brighter lines, due to uncertainties in the continuum level.

In some cases, an emission line may fall within the overlap region of two adjacent filters (see Fig. 1), allowing it to be detected in both filters independently. Duplicated measurements in the catalogue were averaged to improve the S/N, ensuring more robust flux estimates. For filters containing two bright emission lines, individual line fluxes were determined in cases where one of the lines was also detected in the overlap region of an adjacent filter. In such cases, the flux measurement from the overlapping filter was used to disentangle the contributions of the two lines, and the associated uncertainties in the flux measurements were propagated accordingly. Additionally, theoretical line ratios were employed to resolve degeneracies in cases where filters contained multiple emission lines that could not be disentangled solely through measurements. Specifically, we used the theoretical ratios of [O III] λ 5007/[O III] λ 4959 = 2.98

⁴ <https://svo.cab.inta-csic.es>

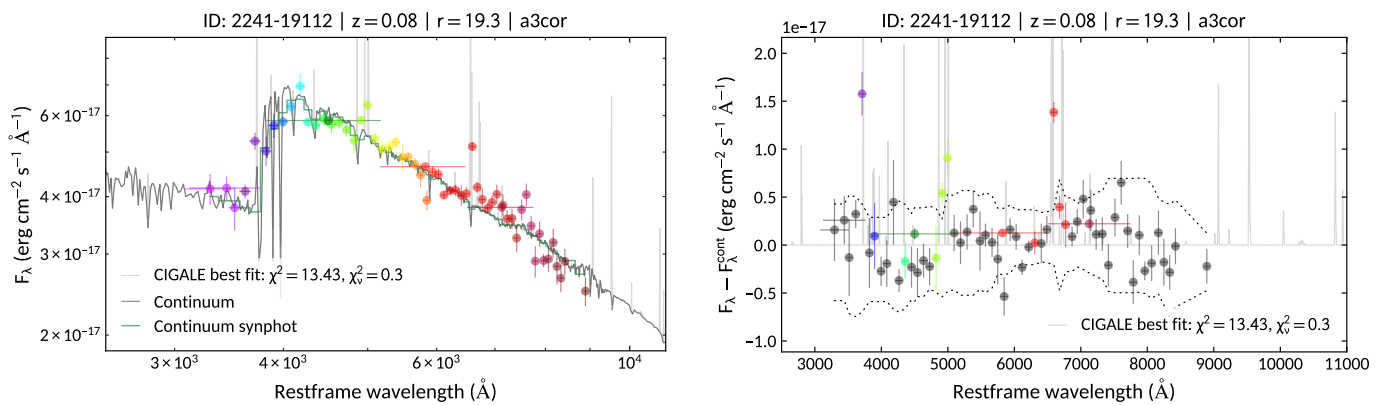


Fig. 3. Extraction of emission-line fluxes from the photospectrum of the galaxy 2241–19112, using the CIGALE best-fit model for the continuum subtraction. *Left:* the observed photospectrum (coloured dots) is compared with the best-fit model (solid light-grey line) and its corresponding continuum (solid dark grey line). The solid green step line indicates the synthetic photometry for the best-fit continuum distribution obtained for the J-PAS filters. *Right:* dots show the continuum-subtracted photospectrum, in colour for filters including lines in Table 1, in grey for continuum filters used in the SED fitting. Dotted black lines indicate the 3σ uncertainty, derived from the scatter in the residual values of the continuum-subtracted photospectrum. The solid light-grey line shows the emission-line spectrum for the CIGALE best-fit model.

and $[\text{N II}]\lambda 6583/[\text{N II}]\lambda 6548 = 2.94$ provided by PYNEB (Luridiana et al. 2015) to estimate the individual line fluxes, corresponding to an electron temperature and density of $T_e = 10^4$ K and $n_e = 100 \text{ cm}^{-3}$, respectively. For instance, flux measurements involving $\text{H}\beta + [\text{O III}]\lambda 4959$, $\text{H}\alpha + [\text{N II}]\lambda 6548$, and $\text{H}\alpha + [\text{N II}]\lambda 6583$ were decomposed into their individual line intensities using these known ratios.

3. Results

The robustness of the method developed to measure emission-line fluxes (Section 2) was tested using simulated observations based on galaxy models with added noise (Section 3.1), synthetic spectrophotometry derived from the DESI spectroscopic survey (Section 3.2), and a comparison between the estimated line fluxes for galaxies in the J-PAS catalogues and available spectroscopic measurements (Section 3.3).

3.1. Comparison with simulated galaxies

A new mock catalogue was generated to simulate J-PAS observations, providing a controlled environment to assess the accuracy of the emission-line flux recovery method and to quantify the uncertainties associated with the SED-fitting procedure itself. Unlike real observations, the use of a mock catalogue allows us to explore a much wider range of physical parameters – such as stellar population age, dust attenuation, metallicity, and emission-line strength – than is accessible with current spectroscopic data. This controlled setup enables us to isolate and characterise the effects of model assumptions (e.g. the choice of stellar population synthesis, dust attenuation law, or parameter sampling) on the recovered fluxes, thus providing a reference framework for interpreting the results obtained from real spectra in Section 3.2. The models were created with the CIGALE code, sampling the redshift range $0 < z < 0.4$, and adopting a configuration independent from that used for fitting, including different stellar population models, dust extinction laws, and parameter grids (see Table A.1). Specifically, the mock catalogue employs the Bruzual & Charlot (2003) models with a Salpeter (1955) initial mass function (IMF) and the Calzetti et al. (2000) dust attenuation law. The parameter values sampled for the mock grid are

entirely different from those in the fitting library, ensuring that no model used for fitting appears among the synthetic inputs. This design not only prevents any overlap between the input and fitting models but also allows us to calibrate how robust the method is at reproducing the continuum around emission lines when the true continuum shape lies completely outside the fitting grid. Finally, the larger number of models in the fitting library, relative to the mock grid, was intended to account for potential numerical degeneracies and model biases during the fitting process. Synthetic photometry was then produced from these models using the J-PAS filter set available in the SVO, and Gaussian noise was stochastically added at a 10% level to reproduce typical observational uncertainties. While a uniform noise level provides a reasonable approximation for most sources, we note that a more detailed noise model – accounting for variations in source magnitude, line equivalent width, and observing conditions – would be more realistic for specific cases. However, for the mock catalogue we adopted a simpler 10% noise level in order to isolate systematics arising solely from the modelling and fitting procedures. The impact of realistic observational noise is taken into account in Sections 3.2 and 3.3, which rely on real DESI and J-PAS observations, respectively.

The synthetic spectra were subsequently processed using the methodology described in Section 2. Specifically, the data were formatted into input tables for CIGALE, with filters containing emission lines masked, both at the peak of the emission and in the transmission wings, to ensure unbiased continuum fitting. These spectra were then fitted with CIGALE using the parameters detailed in Table 2. Following this, the emission-line fluxes were obtained by subtracting the continuum emission and applying the arithmetic procedures outlined in Section 2 to decompose blended fluxes into individual line fluxes.

In Fig. 4, we present the recovered line fluxes for the total $[\text{O III}]\lambda 4959, 5007$ flux and the $\text{H}\alpha + [\text{N II}]\lambda 6548, 6583$ blend. These fluxes are shown as a function of the model input fluxes (Figs 4a and 4b) and the equivalent width values (Figs 4c and 4d). Bright emission lines with fluxes of $\geq 10^{-14} \text{ erg s}^{-1} \text{ cm}^{-2}$ or those relatively bright compared to their continua ($\text{EW} \geq 10 \text{ \AA}$) are recovered with a dispersion ≤ 0.2 dex and without significant bias for EW values above $\sim 20 \text{ \AA}$, as shown in Figs 4c and 4d. However, at low equivalent widths ($\text{EW} \lesssim 10 \text{ \AA}$), a bias of ~ 0.1 –

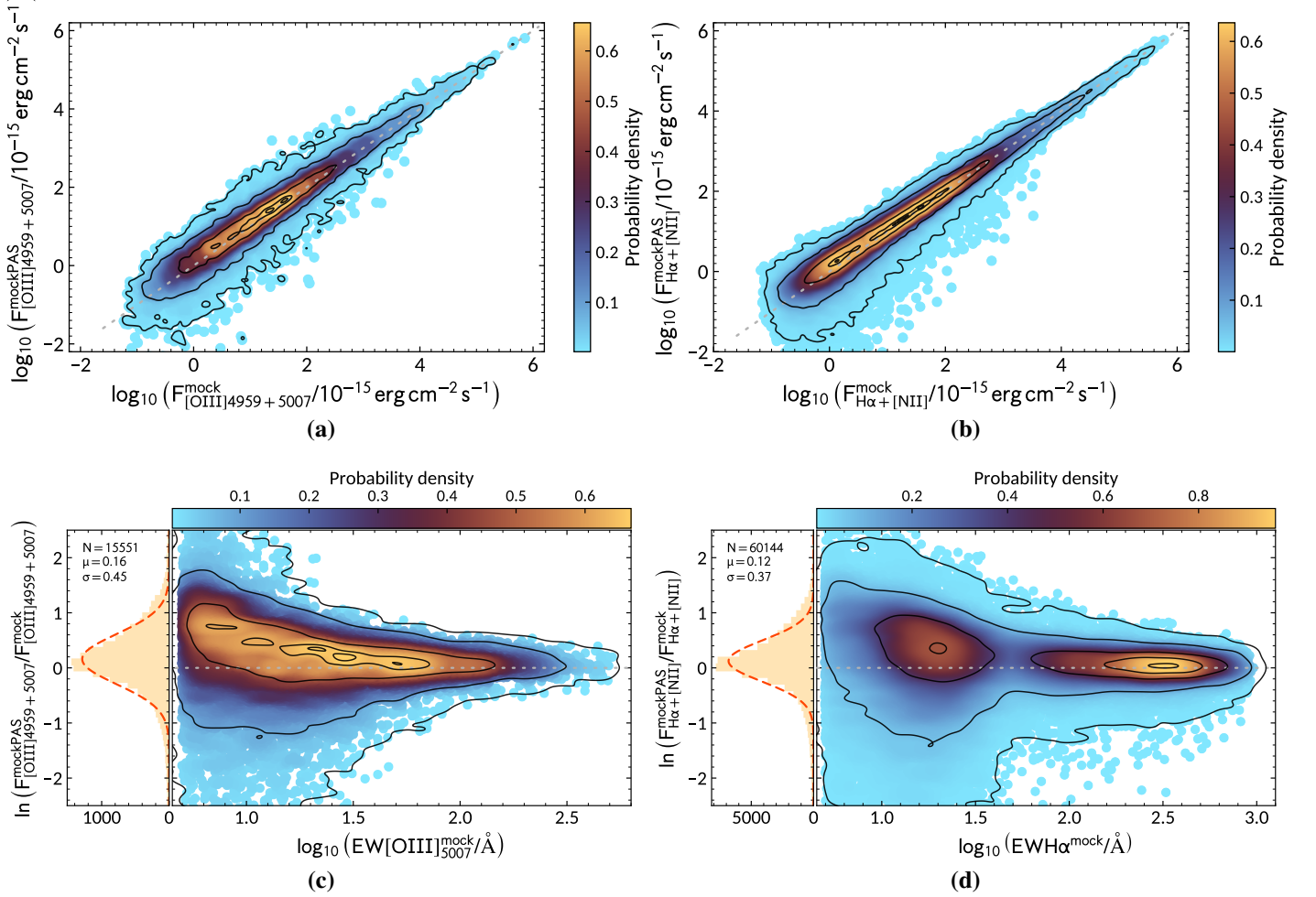


Fig. 4. The upper panels show density plots of the emission-line fluxes for [O III] λ 4959, 5007 (a) and H α + [N II] λ 6548, 6583 (b) derived from the mock catalogue spectra with the J-PAS filter system, using the SED-fitting-based continuum subtraction method described in Section 2. The J-PAS fluxes are compared with the input line fluxes in the mock catalogue. The lower panels show the line flux ratios between the J-PAS line fluxes and the mock input fluxes for [O III] λ 4959, 5007 (c) and H α + [N II] λ 6548, 6583 (d), plotted as a function of the mock equivalent width of [O III] λ 5007 and H α , respectively. In dashed grey style, we show the one-to-one lines in the upper panels and the constant unity value in the lower panels. The side vertical panels in (c) and (d) show the marginal distribution (grey histogram) and the corresponding Gaussian fit (dashed red line) of the J-PAS to mock line flux ratios. In all panels, the black contours represent the 1, 10, 50, 90, and 99% percentiles of the two-dimensional probability distribution.

0.3 towards higher recovered fluxes is observed. This is caused by the loss of contrast between the emission line and the continuum, which increases the uncertainty of the line flux measurement in the narrower filters, challenging the accurate recovery of faint lines blended with the continuum.

Figs 4c and 4d demonstrate that line fluxes with typical uncertainties of 0.3 dex are achieved for most synthetic galaxies with emission lines of $\text{EW} \gtrsim 20 \text{ \AA}$. This result aligns with the detectability threshold of $\text{EW} \gtrsim 25 \text{ \AA}$, empirically derived by Breda et al. (2024) for miniJPAS using polynomial plus Gaussian fitting to extract emission-line fluxes from photospectra. Overall, the results confirm the reliability of the developed method for recovering emission-line fluxes, particularly for lines with high S/N and moderate to large equivalent widths.

3.2. Comparison with DESI synthetic photospectra

As a second test of our methodology, we used real galaxy spectra from the DESI EDR, to generate synthetic J-PAS observations. Specifically, we applied the J-PAS filter transmission curves to

the DESI spectra. This procedure resulted in synthetic J-PAS photospectra, closely mimicking actual observations, but with the benefit of known spectroscopic line fluxes from DESI.

Subsequently, these synthetic photospectra were processed using the same approach described in Section 2: we performed continuum fitting using CIGALE, subtracted the fitted continuum emission, and extracted the fluxes of the brightest emission lines listed in Table 1. The recovered emission-line fluxes were then directly compared with the spectroscopic fluxes provided by the FastSpecFit value-added catalogue (Moustakas et al. 2023; Moustakas et al. in prep.), associated with the DESI EDR.

Fig. 5 illustrates the comparison between the synthetic photometric fluxes derived using our method and the original DESI spectroscopic measurements. The agreement between both datasets is excellent, demonstrating robust flux recovery for emission lines with equivalent widths exceeding $\text{EW} \gtrsim 20 \text{ \AA}$, consistent with the performance observed in the simulated galaxies (Section 3.1). Notably, the ratio of recovered to spectroscopic fluxes in Fig. 5 exhibits a significantly less pronounced bias at low equivalent widths than that seen in the mock catalogue (Fig. 4). We ascribe the more pronounced bias observed in the mock

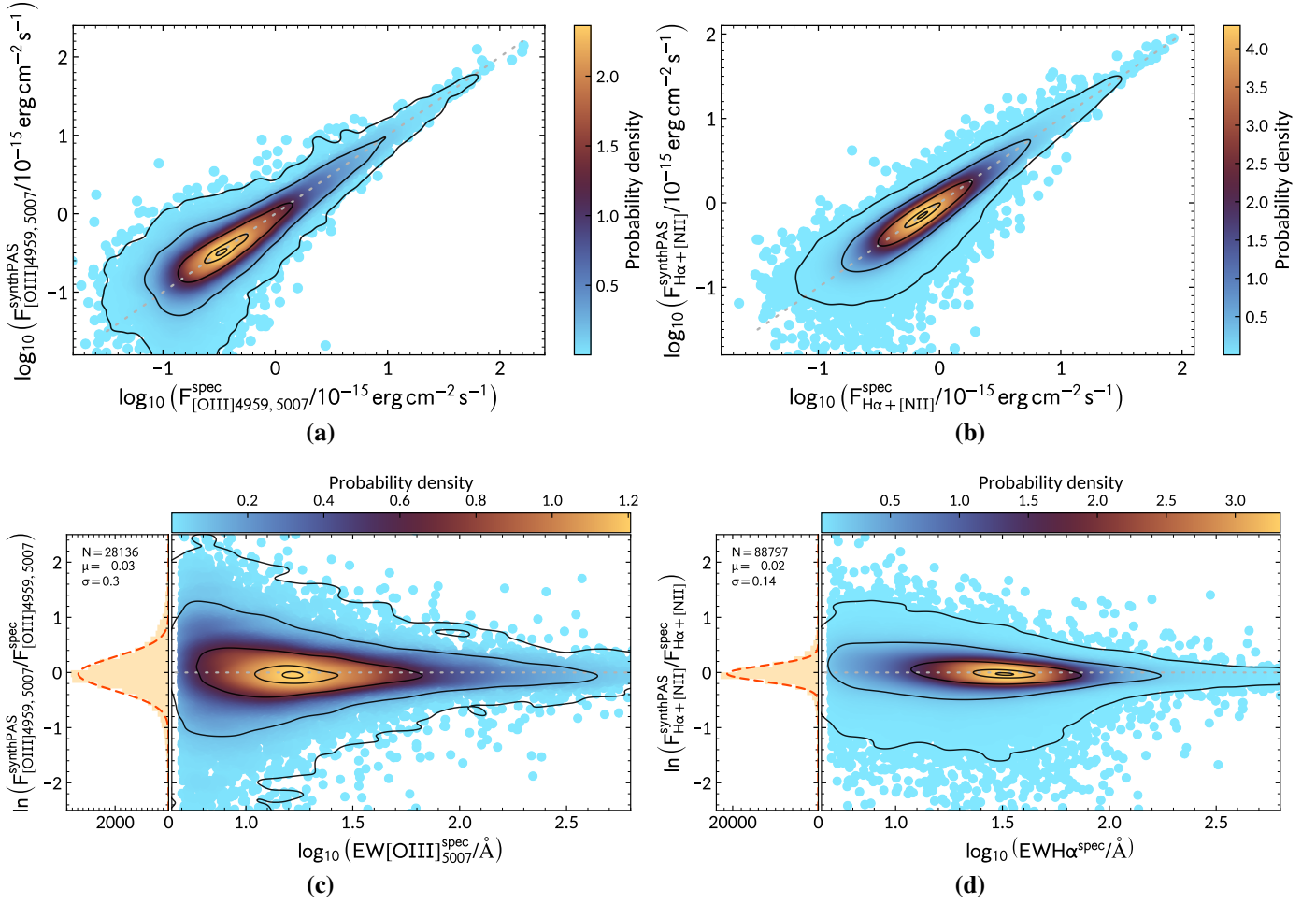


Fig. 5. Same as Fig. 4, but comparing the J-PAS fluxes obtained from the synthetic photometry of DESI EDR spectra with the spectroscopic line fluxes from the FastSpecFit value-added catalogue (Moustakas et al. 2023; Moustakas et al. in prep.). Panels (a) and (b) show the density plots for $[\text{O III}]\lambda 4959, 5007$ and $\text{H}\alpha + [\text{N II}]\lambda 6548, 6583$, respectively. Panels (c) and (d) display the corresponding J-PAS to spectroscopic flux ratios as a function of the spectroscopic equivalent widths.

sample to the large difference in parameter values and continuum shapes between the mock and the SED fitting models. This mismatch limits the fitting model’s ability to provide an accurate estimate of the continuum level, thus affecting flux measurements at low EW values. Conversely, the significantly lower deviation seen in the DESI comparison implies that the parameter space covered by the fitting models is well-suited to the characteristics of a real galaxy sample with varied spectral shapes. Therefore, the test based on synthetic photospectra from DESI confirms that our method for continuum subtraction and line flux extraction introduces no significant biases, validating the reliability and accuracy of the technique when applied to real observational data.

3.3. Comparison with spectroscopic fluxes

After validating our method with the mock catalogue and the DESI synthetic photospectra, we searched for galaxies in the miniJPAS, J-NEP, and J-PAS EDR surveys with available spectroscopic flux measurements in public catalogues. Comparing photometric fluxes derived from narrow-band filters with spectroscopic measurements provides a direct assessment of the accuracy of our methodology. While variations in the apertures used for spectroscopic observations and narrow-band photometry can introduce differences in the line fluxes, these discrepancies are expected to be significant only for extended galaxies. For most

compact sources, typical fibre or slit apertures wider than $\sim 2''$ should yield fluxes comparable to those measured by the $3''$ aperture photometry in miniJPAS, J-NEP, and J-PAS EDR.

Figures 6a and 6b show a comparison between the emission-line fluxes derived from J-PAS photospectra, for galaxies with $i < 21$ mag, and spectroscopic measurements from three external datasets. First, we use the MPA-JHU DR8 value-added catalogue⁵ of the Sloan Digital Sky Survey (SDSS) for galaxies with detected $[\text{O III}]\lambda 4959, 5007$ emission. These fluxes were rescaled using the ratio between the aperture-corrected $\text{H}\alpha$ flux from Duarte Puertas et al. (2017) and the MPA-JHU DR8 $\text{H}\alpha$ measurement, thereby deriving an aperture correction that we then applied consistently to the rest of the SDSS emission lines. Second, we include measurements from the FastSpecFit value-added catalogue (Moustakas et al. 2023; Moustakas et al. in prep.) of the DESI Data Release 1 (DR1; DESI Collaboration et al. 2025). Since FastSpecFit does not provide synthetic i -band fibre magnitudes, but does tabulate the r - and z -band fibre fluxes, we estimated the i -band flux using a first-degree power-law interpolation in wavelength. The DESI line fluxes were then corrected by the ratio between our i -band FLUX_AUTO fluxes and the interpolated i -band flux within the $1''.5$ DESI fibre. Finally, we

⁵ https://www.sdss4.org/dr17/spectro/galaxy_mpa_jhu

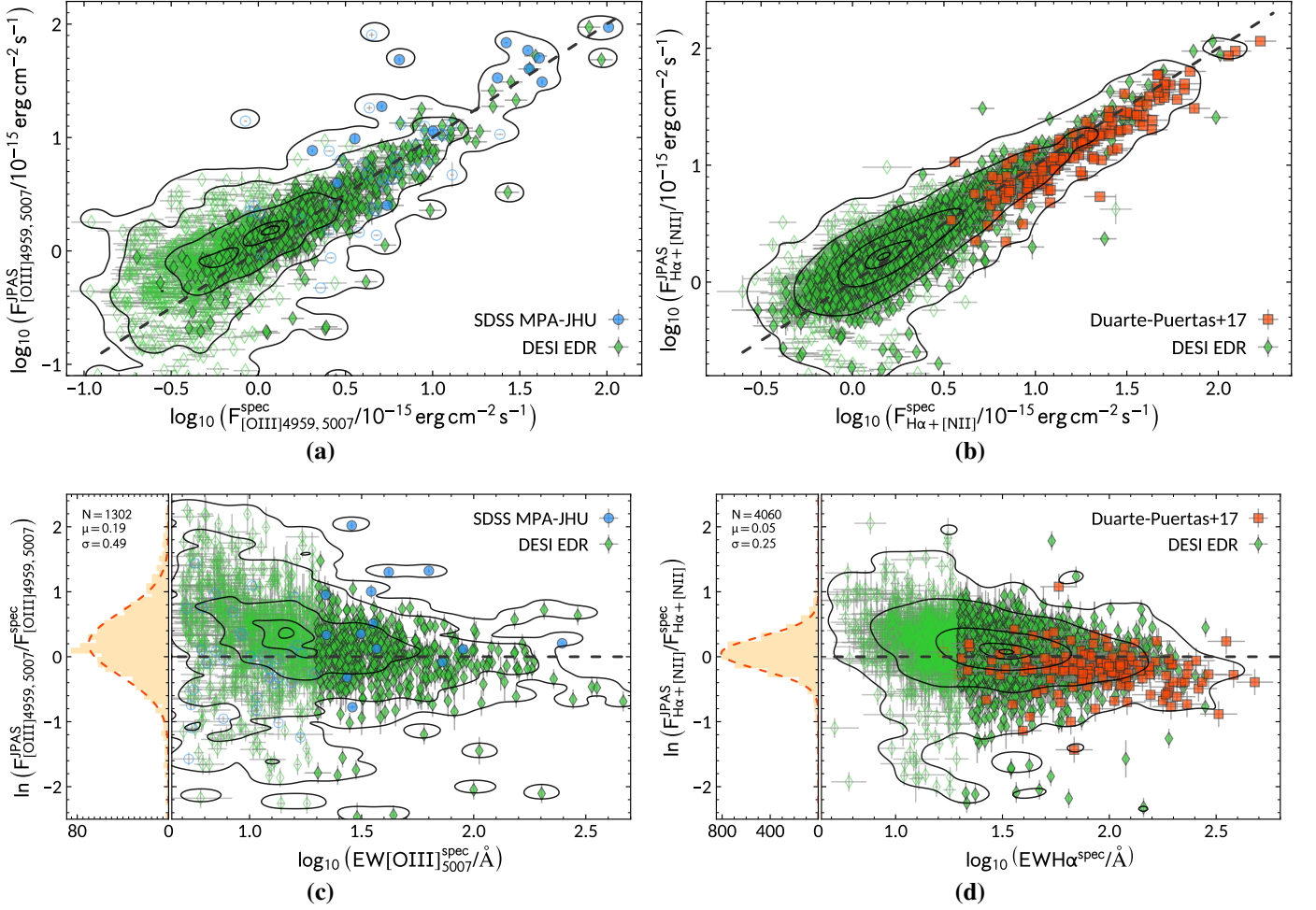


Fig. 6. Same as Fig. 4, but using real miniJPAS, J-NEP and J-PAS EDR photospectra. JOLINES fluxes are compared with SDSS spectroscopic measurements from the MPA-JHU DR8 catalogue (blue circles), aperture-corrected H α fluxes from [Duarte Puertas et al. \(2017\)](#) (red squares), and DESI DR1 line fluxes ([Moustakas et al. 2023](#); [Moustakas et al. in prep.](#); green diamonds). Open and filled symbols denoting EW ranges of 5–20 Å and >20 Å, respectively. Black contours trace the 1, 10, 50, 90, and 99% percentiles.

compare with SDSS galaxies with aperture-corrected H α fluxes from [Duarte Puertas et al. \(2017\)](#), assuming no extinction correction and a $70 \pm 10\%$ contribution of H α to the H α + [N II] blend. The aperture corrections in [Duarte Puertas et al. \(2017\)](#) are based on empirical relations derived from integral-field spectroscopic observations, providing a more reliable basis for comparison with the J-PAS photometric fluxes. Although this approach assumes that the spatial distribution of the line-emitting gas approximately follows that of the stellar continuum, this approximation has been shown to hold, at least to first order, for star-forming galaxies in large samples such as CALIFA ([Iglesias-Páramo et al. 2013, 2016](#)), where the radial growth curves of H α and the r -band continuum show similar trends within the optical extent of the galaxy. This assumption remains valid when the fibre covers a significant fraction of the galaxy, typically above $\sim 20\%$ of its radius, as is the case for most SDSS galaxies at $z \gtrsim 0.04$ ([Kewley et al. 2005](#)). Under this approximation, the continuum-based aperture correction provides a practical means to estimate the total line flux from fibre spectra when no direct spatially resolved emission-line information is available. The lower panels in Fig. 6 show the J-PAS-to-spectroscopic line flux ratios as a function of the equivalent width of [O III] $\lambda 5007$ (Fig. 6c) or H α (Fig. 6d) for a common sample of 1302 and 4060 galaxies, respectively. In all cases, open symbols correspond to measurements with

EW([O III] $\lambda 5007$) (Figs. 6a and 6c) or EW(H α) (Figs. 6b and 6d) in the 5–20 Å range, while filled symbols correspond to galaxies with EW values above 20 Å.

Despite the relatively large uncertainties and scatter in Figs 6a and 6c, the observed trend for the majority of galaxies with bright [O III] $\lambda 4959, 5007$ detections suggests a good agreement between the J-PAS spectrophotometric fluxes and the spectroscopic values, especially at large EW([O III] $\lambda 5007$) values. This is confirmed by the larger sample of common sources with H α + [N II] $\lambda 6548, 6583$ measurements in Figs 6b and 6d. Overall, galaxies with spectroscopic fluxes above $\gtrsim 2 \times 10^{-15} \text{ erg s}^{-1} \text{ cm}^{-2}$ show a good agreement with J-PAS measurements, with a significant decrease in the scatter for sources with EW(H α) > 20 Å (filled symbols), as predicted by results obtained for the simulated photospectra (Section 3.1). A small bias towards larger J-PAS fluxes is noticeable for galaxies with EWs in the 5–20 Å range, which is partially attributable to uncorrected differences in the flux extraction apertures.

In Figure 7, we show the ability of our method to recover the fluxes of other relevant lines in the optical spectrum, namely the [O II] $\lambda 3726, 3729$ and [S II] $\lambda 6716, 6731$ doublets, and the [N II] $\lambda 6583$ line. The latter was derived from the filters containing the H α + [N II] $\lambda 6548$ and H α + [N II] $\lambda 6583$ blends, by assuming a $\sim 22\%$ contribution from the [N II] $\lambda 6583$ line to the

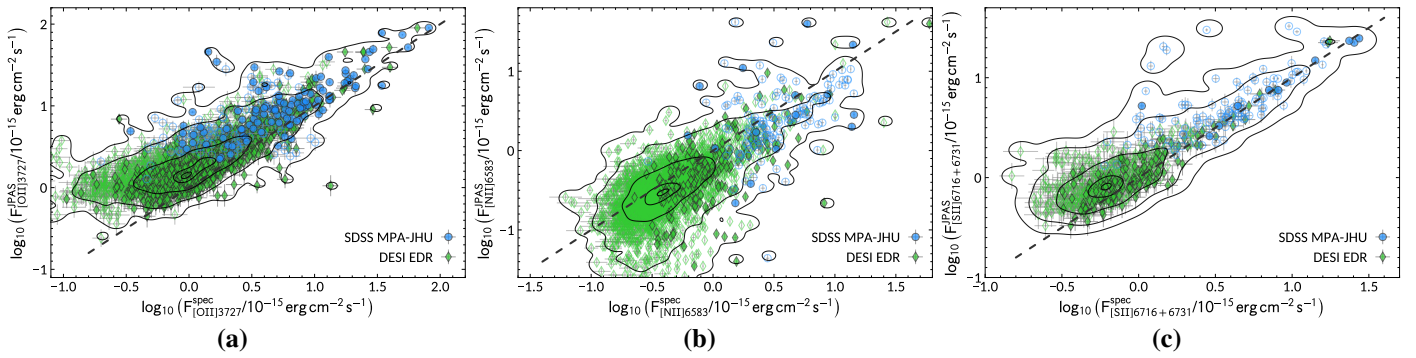


Fig. 7. Emission-line fluxes for [O II]λ3726, 3729 (a), [N II]λ6583 (b), and [S II]λ6716, 6731 (c) derived from the miniJPAS, J-NEP and J-PAS EDR photospectra. JOLINES fluxes are compared with SDSS spectroscopic measurements from the MPA-JHU DR8 catalogue (blue circles; rescaled using the aperture-corrected H α fluxes from Duarte Puertas et al. 2017) and DESI DR1 line fluxes (Moustakas et al. 2023; Moustakas et al. in prep.; green diamonds). For panel (b), a $\sim 22\%$ contribution of [N II]λ6583 to the H α + [N II] blend is assumed. Open and filled symbols denote equivalent widths of 5–20 Å and > 20 Å, respectively. Dashed grey lines mark the one-to-one relation, and black contours indicate the 1, 10, 50, 90, and 99% percentiles of the two-dimensional probability distribution.

total H α + [N II]λ6548, 6583 flux, and adopting the theoretical [N II]λ6583/[N II]λ6548 ratio of 2.94 (for $T_e = 10^4$ K and $n_e = 100$ cm $^{-3}$; Luridiana et al. 2015). In all three cases, the emission-line fluxes are successfully recovered, with a small bias towards slightly higher fluxes in J-PAS at lower flux or equivalent width values. The median and dispersion of the ratios between the J-PAS and spectroscopic flux measurements are 0.8 ± 0.2 for [O II], 1.5 ± 0.7 for [N II], and 1.0 ± 0.3 for [S II], indicating a generally good agreement within the expected uncertainties. The successful recovery of the [N II]λ6583 flux in this figure demonstrates the capability of the J-PAS narrow-band system to separate blended features and recover individual emission-line fluxes. This is achieved by combining the information from adjacent filters and relying on only minimal theoretical assumptions, highlighting the potential of the method to retrieve, for example, H α fluxes decontaminated from [N II] or individual [O III] and H β fluxes. This implies that robust galaxy selections based on these emission lines can be performed, enabling the construction of large samples of galaxies with, for example, high N/O ratios using the [N II]λ6583/[O II]λ3727 ratio, strong ionising radiation fields traced by the [O III]λ5007/[O II]λ3727 ratio, or active nuclei identified through diagnostic ratios such as [O III]λ5007/H β and [S II]λ6716, 6731/H α .

Overall, the comparison with line spectroscopic fluxes suggests that the continuum-subtraction method based on SED fitting described in Section 2 is capable of reliably recovering emission-line fluxes from galaxy photospectra in miniJPAS, J-NEP, and J-PAS EDR. These results further validate the robustness of the photometric approach for detecting and measuring emission lines in compact galaxies with sufficient flux strength. See Section 5 for a detailed discussion on the overall properties of emission-line galaxies included in the JOLINES catalogue and the implications of these results for future surveys.

4. Emission-line flux catalogue

In this section, we provide a description of the JOLINES value-added catalogue, which contains emission-line fluxes for all galaxies in the miniJPAS, J-NEP, and J-PAS EDR surveys in its first release. The catalogue serves as a foundational resource for analysing emission-line galaxies within these surveys and is designed to be expanded in future releases. As the J-PAS sur-

vey progresses, JOLINES will be updated to include emission-line fluxes derived from the photospectra of galaxies observed in forthcoming data releases, ensuring the catalogue remains a comprehensive and up-to-date tool for galaxy evolution studies.

The JOLINES catalogue is structured to provide key information for each galaxy, including the TILE-ID and NUMBER identifiers assigned by the miniJPAS, J-NEP, or J-PAS EDR catalogues, the galaxy coordinates in right ascension and declination, as well as the spectrophotometric redshifts. Additionally, it includes the emission-line fluxes or line blends available for each target, and their associated uncertainties. Certain line blends, such as H β + [O III]λ4959, are only present at specific redshifts, depending on the filter configuration and the rest-frame wavelengths of the lines. When possible, the catalogue provides individual line fluxes, which are disentangled using theoretical line ratios and fluxes from adjacent filters, as described in Section 2. This ensures that the information is as complete and accurate as possible for a wide range of galaxies and redshifts.

For cases where individual line fluxes are measured for lines close in wavelength, that may be blended for other targets at different redshift such as H β + [O III]λ4959, the catalogue also includes the total line blend flux for completeness. Flux measurements from filters contaminated by adjacent emission lines in their transmission wings have been corrected. However, these measurements are flagged to indicate possible large uncertainties. These are primarily caused by wavelength shifts in the transmission profiles (of the order of 10–15 Å) due to spatial variations across the field of view, which can affect the net transmission for emission lines in the filter side.

The current JOLINES catalogue, covering miniJPAS, J-NEP, and J-PAS EDR, comprises approximately 13 900 sources with significant emission ($> 3\sigma$) in the H α + [N II]λ6548, 6583 blend. Additionally, the catalogue includes 6 100 detections in [O II]λ3727, 1 700 in [Ne III]λ3869, 2 900 in H β , 7 200 sources in [O III]λ5007, 500 in [O I]λ6300, 6 100 in H α , and 4 000 in [S II]λ6724. For a comprehensive list and description of all data columns included in the JOLINES catalogue, refer to Table 1 in Appendix B. The JOLINES catalogue can be found in the online version of this publication and is also distributed as a value-added product alongside the official data releases of the miniJPAS⁶, J-

⁶ https://www.j-pas.org/datareleases/miniJPAS_public_data_release_pdr201912

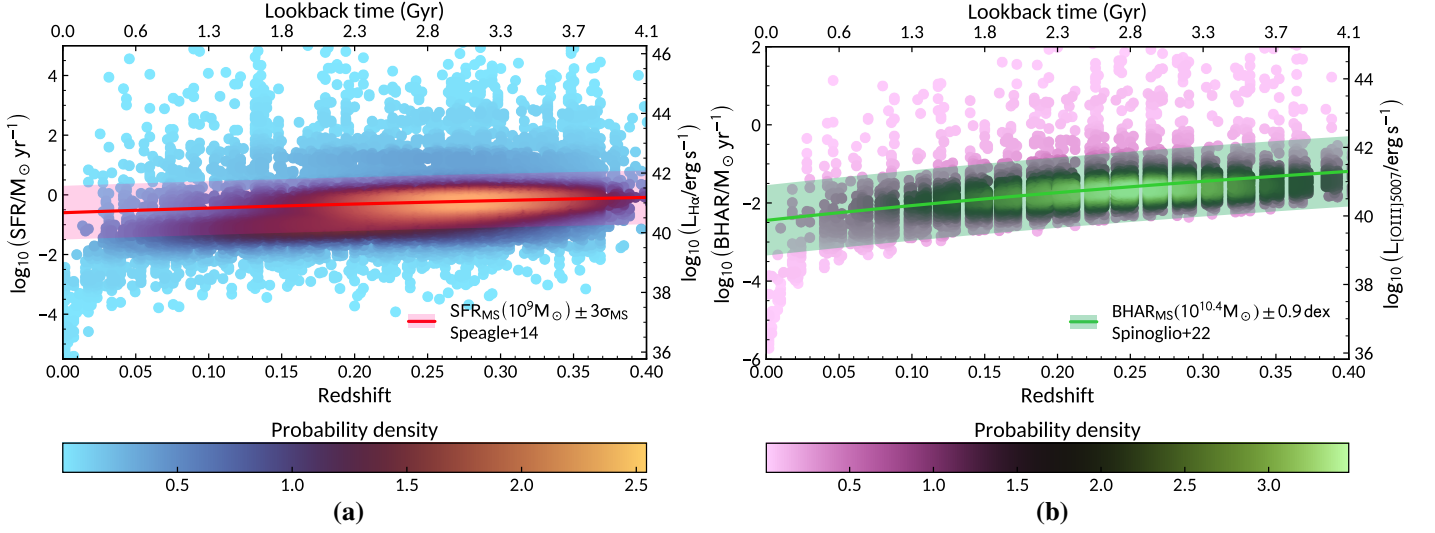


Fig. 8. Distribution of SFR as a function of redshift (a) for galaxies detected in miniJPAS, J-NEP, and J-PAS EDR, determined from their extinction-corrected H α emission (Kennicutt & Evans 2012). The evolution of the main sequence for a galaxy with $M_* = 10^9 M_\odot$ and its associated dispersion are shown for comparison (solid line and shaded area in red colour; Speagle et al. 2014). Evolution of BHAR as a function of redshift (b), derived from the extinction-corrected [O III] λ 5007 luminosity (Spinoglio et al. 2024). The SFR–BHAR relation for an AGN galaxy with $M_* = 10^{10.4} M_\odot$, obtained for AGN in the nearby Universe, is also shown (solid line and shaded area in green colour; Spinoglio et al. 2022).

NEP⁷, and the J-PAS EDR⁸ surveys. It can be accessed through their respective data portals, providing an easily available resource for the astronomical community.

5. Discussion

As shown by the analysis in Section 3, the JOLINES catalogue comprises emission-line galaxies with at least one bright emission line exhibiting an equivalent width of $\gtrsim 10\text{--}20 \text{ \AA}$ within the redshift range $0 < z < 0.4$. This threshold predominantly selects star-forming galaxies, AGN, and composite sources, defining a sample that is particularly well suited for studying the evolution of these phenomena in the local Universe (e.g. González Delgado et al. 2022; Rodríguez-Martín et al. 2022; López et al. 2023). In this section, our aim is to provide a general overview of the expected properties for the sample of galaxies included in the JOLINES catalogue.

The most prominent lines detected for star-forming galaxies and AGN are typically H α and [O III] λ 5007, respectively, which show median luminosities and associated dispersions of $\log(L_{\text{H}\alpha}/\text{erg s}^{-1}) \sim 40.8 \pm 0.9$ and $\log(L_{[\text{O III}]\lambda 5007}/\text{erg s}^{-1}) \sim 40.8 \pm 0.6$. These have been corrected for dust extinction using the Balmer decrement (H α /H β) measured in JOLINES, assuming an intrinsic ratio of 2.87, consistent with Case B recombination in Osterbrock & Ferland (2006). To distinguish star-forming galaxies from those with a significant AGN contribution, we classify as AGN those sources with $\text{EW}([\text{O III}]\lambda 5007) \geq 5 \text{ \AA}$ and satisfying at least one of the following conditions: $[\text{O III}]\lambda 5007/\text{H}\beta \geq 5$, $[\text{S II}]\lambda 6725/\text{H}\alpha \geq 0.55$, $[\text{O I}]\lambda 6300/\text{H}\alpha \geq 0.08$, or $[\text{O III}]\lambda 5007/[\text{O II}]\lambda 3727 \geq 2$ (e.g. Kewley et al. 2006; Stasińska et al. 2025). We note that AGN continuum emission has not been included in the SED fitting, however, only powerful Type 1 AGN are expected to noticeably affect the continuum in the wavelength and redshift range probed here. In such cases

the continuum would appear as a bluer power-law, which the model would compensate by adding a larger fraction of young, blue stars, but the overall continuum level would remain comparable, and the resulting emission-line flux measurements would not be significantly affected (see Fig. C.1 and discussion in Appendix C).

An EW threshold of $\gtrsim 10\text{--}20 \text{ \AA}$ in H α strongly favours galaxies undergoing recent star formation episodes, typically within the last $\lesssim 10 \text{ Myr}$, with SFR in the $0.1\text{--}2 M_\odot \text{ yr}^{-1}$ range, as estimated from the median extinction-corrected H α luminosity and its associated dispersion in our sample (Kennicutt & Evans 2012). These values are characteristic of main-sequence galaxies with stellar masses close to the knee of the stellar mass function (Noeske et al. 2007; Elbaz et al. 2007, 2011; Duarte Pueras et al. 2017). In this regard, Fig. 8a shows the distribution of SFR in our sample as a function of redshift, excluding the AGN population. The general trend aligns with the star-forming main sequence evolution for galaxies with a stellar mass around $M_* = 10^9 M_\odot$ (solid line and shaded area in red; Speagle et al. 2014), suggesting that JOLINES predominantly captures galaxies actively forming stars. This is in agreement with the results obtained by Martínez-Solaesche et al. (2022), who employed machine learning techniques to analyse the miniJPAS sample (see also results by Favole et al. 2024, based on spectroscopic data). At higher redshifts, approaching $z \sim 0.4$, the general increase in SFR and correspondingly higher EW(H α) values (e.g. Fumagalli et al. 2012) facilitate the detection of slightly less massive galaxies in JOLINES. Additionally, the catalogue includes a small fraction of dwarf galaxies with elevated sSFR ($\gtrsim 3 \text{ Gyr}^{-1}$) and exceptionally high EW([O III] λ 5007) or EW(H α) values of $\gtrsim 300 \text{ \AA}$ (Iglesias-Páramo et al. 2022; Lumberras-Calle et al. 2022; Giménez-Alcázar in prep.), which are often associated with intense starburst episodes in low-metallicity galaxies.

On the other hand, the [O III] λ 5007 line allows us to detect a significant fraction of the Seyfert galaxy population at low redshift, which exhibits a characteristic luminosity of $\log(L_{[\text{O III}]\lambda 5007}^*/\text{erg s}^{-1}) \sim 41.4$ at the knee of the [O III] λ 5007 luminosity function (Bongiorno et al. 2010). Figure 8b shows the

⁷ <https://archive.cefca.es/catalogues/jnep-pdr202107>

⁸ <https://archive.cefca.es/catalogues/jpas-edr>

black hole accretion rate (BHAR) as a function of redshift for an active galaxy with $M_* = 10^{10.4} M_\odot$, derived from the BHAR–SFR correlation found in nearby AGN (Spinoglio et al. 2022), using the extinction-corrected $[O\text{ III}]\lambda 5007$ luminosity as a proxy for the BHAR (Spinoglio et al. 2024):

$$\frac{\text{BHAR}}{M_\odot \text{ yr}^{-1}} = \frac{L_{\text{bol}}}{\eta c^2} \approx 10^{-36.5 \pm 0.2} \times \left(\frac{L_{[O\text{ III}]\lambda 5007}}{\text{erg s}^{-1}} \right)^{0.88 \pm 0.05} \quad (1)$$

assuming a radiative efficiency of $\eta = 0.1$. The observed distribution of $\log(L_{[O\text{ III}]\lambda 5007})$ with redshift in Fig. 8b indicates that JOLINES includes a significant fraction of moderately luminous AGN, consistent with known relationships between BHAR and SFR in local active galaxies.

Finally, we highlight that other galaxy populations, such as low-luminosity AGN, numerous in the nearby Universe (Ho 2008; Burke et al. 2025), are expected to be detected through their characteristic strong low-ionisation emission lines (Heckman 1980). A rough comparison between the median extinction-corrected luminosities for transitions from low-ionisation species in JOLINES (e.g. $\log(L_{[O\text{ II}]\lambda 3727}/\text{erg s}^{-1}) \sim 40.9 \pm 0.5$) and the characteristic line luminosities at the knee of the luminosity functions for these nuclei ($\log(L_{[O\text{ II}]\lambda 3727}^*/\text{erg s}^{-1}) \sim 40.5$; Favole et al. 2024), suggests that JOLINES is also expected to include a significant fraction of low-luminosity AGN.

These findings underscore the capability of JOLINES to capture a diverse population of galaxies, spanning a wide range of star formation and AGN activity, thereby providing a valuable resource for studying galaxy evolution at low redshift.

6. Summary

In this study, we introduced the JOLINES value-added catalogue, a dataset containing emission-line fluxes for galaxies in the miniJPAS and J-NEP precursor surveys, and in the J-PAS EDR. The catalogue is constructed using a robust SED-fitting approach with CIGALE, which allows accurate determination of the continuum emission and precise measurement of line fluxes from narrow-band photometry. This methodology is crucial for obtaining reliable emission-line fluxes, as direct continuum subtraction can introduce significant uncertainties, particularly for faint lines.

The accuracy of our method was tested using simulated galaxy spectra with added noise, allowing us to assess how well individual and blended emission-line fluxes can be recovered. We find that our approach successfully retrieves line fluxes with minimal bias, particularly for lines with equivalent widths $EW \gtrsim 20 \text{ \AA}$. Additionally, we performed a comparison with spectroscopic measurements from SDSS and DESI, confirming that emission-line fluxes derived from J-PAS photospectra are consistent with spectroscopic values, with a typical dispersion of ~ 0.3 dex for bright lines. The agreement improves for stronger emission lines, reinforcing the reliability of the method for star-forming and AGN-host galaxies.

The JOLINES catalogue includes galaxy identifiers, sky coordinates, spectro-photometric redshifts, and emission-line fluxes or blends for each target. Line blends, such as $H\beta + [O\text{ III}]\lambda 4959$, are included when present, and individual line fluxes are provided where possible using theoretical line ratios and measurements from adjacent filters. Flux measurements affected by contamination from nearby lines in the filter transmission wings are corrected but remain flagged due to residual uncertainties. The first JOLINES release provides statistically robust samples for the brightest optical emission lines, including approximately 13 900 galaxies with significant detections in the $H\alpha + [N\text{ II}]$ complex,

7 200 in $[O\text{ III}]\lambda 5007$, 6 100 in $[O\text{ II}]\lambda 3727$, 2 900 in $H\beta$, and 4 000 in $[S\text{ II}]\lambda 6716, 6731$, among others. These large samples enable population-wide studies across the full sample of galaxies in J-PAS surveys.

This catalogue is publicly available as part of the miniJPAS, J-NEP, and J-PAS EDR data releases and will be continuously updated with future J-PAS data. By providing a robust dataset for emission-line galaxies, JOLINES will enable statistical studies of star formation, AGN activity, and the interstellar medium across a wide range of galaxy populations.

Acknowledgements. Based on observations made with the JST250 telescope and JPCam at the Observatorio Astrofísico de Javalambre (OAJ), in Teruel, owned, managed, and operated by the Centro de Estudios de Física del Cosmos de Aragón (CEFCA). This paper has gone through internal review by the J-PAS collaboration. JAFO acknowledges financial support by the Spanish Ministry of Science and Innovation (MCIN/AEI/10.13039/501100011033), by “ERDF A way of making Europe” and by “European Union NextGenerationEU/PRTR” through the grants PID2021-124918NB-C44 and CNS2023-145339; MCIN and the European Union – NextGenerationEU through the Recovery and Resilience Facility project ICTS-MRR-2021-03-CEFCA. RMGD acknowledges financial support from the Severo Ochoa grant CEX2021-001131-S funded by MICIU/AEI/10.13039/501100011033, and from the project PID2022-141755NB-I00. RA, AHC and JZC, acknowledge support of grant PID2023-147386NB-I00, funded by MICIU/AEI/10.13039/501100011033 and by ERDF/EU. IB has received funding from the European Union’s Horizon 2020 research and innovation programme under the Marie Skłodowska–Curie Grant Agreement No. 101059532. We acknowledge the OAJ Data Processing and Archiving Department (DPAD) for reducing and calibrating the OAJ data used in this work. Funding for the J-PAS Project has been provided by the Governments of Spain and Aragón through the Fondo de Inversiones de Teruel; the Aragonese Government through the Research Groups E96, E103, E16_17R, E16_20R, and E16_23R; the Spanish Ministry of Science and Innovation (MCIN/AEI/10.13039/501100011033 and “ERDF A way of making Europe”) with grants PID2021-124918NB-C41, PID2021-124918NB-C42, PID2021-124918NA-C43, and PID2021-124918NB-C44; the Spanish Ministry of Science, Innovation and Universities (MICIU/AEI/FEDER, UE) with grants PGC2018-097585-B-C21 and PGC2018-097585-B-C22; the Spanish Ministry of Economy and Competitiveness (MINECO) under AYA2015-66211-C2-1-P, AYA2015-66211-C2-2, and AYA2012-30789; and European FEDER funding (FCDD10-4E-867, FCDD13-4E-2685). The Brazilian agencies FINEP, FAPESP, FAPERJ and the National Observatory of Brazil have also contributed to this project. Additional funding was provided by the Tartu Observatory and by the J-PAS Chinese Astronomical Consortium. This research has made use of the SVO Filter Profile Service “Carlos Rodrigo”, funded by MCIN/AEI/10.13039/501100011033/ through grant PID2020-112949GB-I00. This work made use of *ASTROPY*⁹; a community-developed core Python package and an ecosystem of tools and resources for astronomy (Astropy Collaboration et al. 2022).

References

- Arnouts, S. & Ilbert, O. 2011, LePHARE: Photometric Analysis for Redshift Estimate, Astrophysics Source Code Library, record ascl:1108.009
- Astropy Collaboration, Price-Whelan, A. M., Lim, P. L., et al. 2022, *ApJ*, 935, 167
- Baldwin, J. A., Phillips, M. M., & Terlevich, R. 1981, *PASP*, 93, 5
- Benitez, N., Dupke, R., Moles, M., et al. 2014, arXiv e-prints, arXiv:1403.5237
- Bongiorno, A., Mignoli, M., Zamorani, G., et al. 2010, *A&A*, 510, A56
- Bonoli, S., Marín-Franch, A., Varela, J., et al. 2021, *A&A*, 653, A31
- Boquien, M., Burgarella, D., Roehlly, Y., et al. 2019, *A&A*, 622, A103
- Breda, I., Amantidis, S., Vilchez, J. M., et al. 2024, *MNRAS*, 528, 3340
- Bruzual, G. & Charlot, S. 2003, *MNRAS*, 344, 1000
- Burke, C. J., Natarajan, P., Baldassare, V. F., & Geha, M. 2025, *ApJ*, 978, 77
- Calzetti, D., Armus, L., Bohlin, R. C., et al. 2000, *ApJ*, 533, 682
- Cardelli, J. A., Clayton, G. C., & Mathis, J. S. 1989, *ApJ*, 345, 245
- Cardoso, L. S. M., Gomes, J. M., Papaderos, P., et al. 2022, *A&A*, 667, A11
- Cenarro, A. J., Moles, M., Cristóbal-Hornillos, D., et al. 2019, *A&A*, 622, A176
- Chabrier, G. 2003, *PASP*, 115, 763
- Charlot, S. & Fall, S. M. 2000, *ApJ*, 539, 718
- Cook, D. O., Kasliwal, M. M., Van Sistine, A., et al. 2019, *ApJ*, 880, 7
- Dawson, J. M., Davis, T. A., Gomez, E. L., & Schock, J. 2021, *MNRAS*, 503, 574

⁹ <http://www.astropy.org>

- DESI Collaboration, Abdul-Karim, M., Adame, A. G., et al. 2025, arXiv e-prints, arXiv:2503.14745
- DESI Collaboration, Adame, A. G., Aguilar, J., et al. 2024, AJ, 168, 58
- Dhar, S. & Shamir, L. 2022, Astronomy and Computing, 38, 100545
- Dickson, R., Tadhunter, C., Shaw, M., Clark, N., & Morganti, R. 1995, MNRAS, 273, L29
- Duarte Puertas, S., Vilchez, J. M., Iglesias-Páramo, J., et al. 2017, A&A, 599, A71
- Elbaz, D., Daddi, E., Le Borgne, D., et al. 2007, A&A, 468, 33
- Elbaz, D., Dickinson, M., Hwang, H. S., et al. 2011, A&A, 533, A119
- Favole, G., Gonzalez-Perez, V., Ascasibar, Y., et al. 2024, A&A, 683, A46
- Fumagalli, M., Patel, S. G., Franx, M., et al. 2012, ApJ, 757, L22
- González Delgado, R. M., Díaz-García, L. A., de Amorim, A., et al. 2021, A&A, 649, A79
- González Delgado, R. M., Rodríguez-Martín, J. E., Díaz-García, L. A., et al. 2022, A&A, 666, A84
- Heckman, T. M. 1980, A&A, 87, 152
- Hernán-Caballero, A., Akhlaghi, M., López-Sanjuan, C., et al. 2024, A&A, 684, A61
- Hernán-Caballero, A., Varela, J., López-Sanjuan, C., et al. 2021, A&A, 654, A101
- Hernán-Caballero, A., Willmer, C. N. A., Varela, J., et al. 2023, A&A, 671, A71
- Ho, L. C. 2008, ARA&A, 46, 475
- Holt, J., Tadhunter, C. N., González Delgado, R. M., et al. 2007, MNRAS, 381, 611
- Huertas-Company, M. & Lanusse, F. 2023, PASA, 40, e001
- Iglesias-Páramo, J., Arroyo, A., Kehrig, C., et al. 2022, A&A, 665, A95
- Iglesias-Páramo, J., Vilchez, J. M., Galbany, L., et al. 2013, A&A, 553, L7
- Iglesias-Páramo, J., Vilchez, J. M., Rosales-Ortega, F. F., et al. 2016, ApJ, 826, 71
- Jalan, P., Khaire, V., Vivek, M., & Gaikwad, P. 2024, A&A, 688, A126
- Kennicutt, R. C. & Evans, N. J. 2012, ARA&A, 50, 531
- Kewley, L. J., Dopita, M. A., Sutherland, R. S., Heisler, C. A., & Trevena, J. 2001, ApJ, 556, 121
- Kewley, L. J., Groves, B., Kauffmann, G., & Heckman, T. 2006, MNRAS, 372, 961
- Kewley, L. J., Jansen, R. A., & Geller, M. J. 2005, PASP, 117, 227
- Kewley, L. J., Nicholls, D. C., & Sutherland, R. S. 2019, ARA&A, 57, 511
- Lee, J. C., Ly, C., Spitler, L., et al. 2012, PASP, 124, 782
- Leung, H. W. & Bovy, J. 2019, MNRAS, 483, 3255
- Logroño-García, R., Vilella-Rojo, G., López-Sanjuan, C., et al. 2019, A&A, 622, A180
- López, I. E., Brusa, M., Bonoli, S., et al. 2023, A&A, 672, A137
- Lumbreras-Calle, A., López-Sanjuan, C., Sobral, D., et al. 2022, A&A, 668, A60
- Luridiana, V., Morisset, C., & Shaw, R. A. 2015, A&A, 573, A42
- Ly, C., Malkan, M. A., Kashikawa, N., et al. 2007, ApJ, 657, 738
- Martínez-Solaache, G., González Delgado, R. M., García-Benito, R., et al. 2021, A&A, 647, A158
- Martínez-Solaache, G., González Delgado, R. M., García-Benito, R., et al. 2022, A&A, 661, A99
- Mejía-Narváez, A., Bruzual, G., Magris, C. G., et al. 2017, MNRAS, 471, 4722
- Moustakas, J., Buhler, J., Scholte, D., Dey, B., & Khederlarian, A. 2023, FastSpecFit: Fast spectral synthesis and emission-line fitting of DESI spectra, Astrophysics Source Code Library, record ascl:2308.005
- Nakajima, K., Ouchi, M., Shimasaku, K., et al. 2012, ApJ, 745, 12
- Noeske, K. G., Weiner, B. J., Faber, S. M., et al. 2007, ApJ, 660, L43
- Osterbrock, D. E. & Ferland, G. J. 2006, Astrophysics of gaseous nebulae and active galactic nuclei (University Science Books)
- Rahna, P. T., Akhlaghi, M., López-Sanjuan, C., et al. 2025, A&A, 695, A200
- Reines, A. E., Nidever, D. L., Whelan, D. G., & Johnson, K. E. 2010, ApJ, 708, 26
- Rhea, C., Rousseau-Nepton, L., Prunet, S., et al. 2021, ApJ, 910, 129
- Rodrigo, C. & Solano, E. 2020, in XIV.0 Scientific Meeting (virtual) of the Spanish Astronomical Society, 182
- Rodrigo, C., Solano, E., & Bayo, A. 2012, SVO Filter Profile Service Version 1.0, IVOA Working Draft 15 October 2012
- Rodríguez-Martín, J. E., González Delgado, R. M., Martínez-Solaache, G., et al. 2022, A&A, 666, A160
- Salpeter, E. E. 1955, ApJ, 121, 161
- Salzer, J. J., Carr, D. J., Sieben, J., Brunker, S. W., & Hirschauer, A. S. 2023, AJ, 166, 81
- Solórzano-Iñarrea, C., Best, P. N., Röttgering, H. J. A., & Cimatti, A. 2004, MNRAS, 351, 997
- Speagle, J. S., Steinhardt, C. L., Capak, P. L., & Silverman, J. D. 2014, ApJS, 214, 15
- Spinoglio, L., Fernández-Ontiveros, J. A., & Malkan, M. A. 2022, ApJ, 941, 46
- Spinoglio, L., Fernández-Ontiveros, J. A., & Malkan, M. A. 2024, ApJ, 964, 117
- Stasińska, G., Vale Asari, N., Wójtowicz, A., & Kozieł-Wierzbowska, D. 2025, A&A, 693, A135
- Ucci, G., Ferrara, A., Pallottini, A., & Gallerani, S. 2018, MNRAS, 477, 1484
- Vilella-Rojo, G., Viironen, K., López-Sanjuan, C., et al. 2015, A&A, 580, A47

Appendix A: Mock catalogue parameters

Table A.1. Parameters and their respective sampling ranges for the various modules used to generate the mock catalogue with CIGALE, used in Section 3 to test the reliability of the method developed to obtain emission-line fluxes from the narrow-band spectrophotometric data.

Parameters	Sampling range
<i>Star formation history: delayed model</i>	
Age of the main population	7, 8, 9 Gyr
e-folding time	1, 2 Gyr
Age of the young burst	8, 20, 80, 150, 300, 500 Myr
e-folding time young burst	2, 5 Myr
Burst stellar mass fraction	0.01, 0.05, 0.1
<i>Simple Stellar populations: Bruzual & Charlot (2003)</i>	
Initial Mass Function	Salpeter (1955)
Metallicity	0.004, 0.008, 0.02, 0.05
<i>Nebular emission</i>	
Ionisation parameter ($\log U$)	-3.0, -3.3, -3.5, -3.7, -4.0
Gas metallicity (Z_{gas})	0.001, 0.004, 0.014, 0.022, 0.041
Electron density (n_e)	100 cm^{-3}
<i>Dust extinction</i>	
Dust attenuation law	modified Calzetti et al. (2000)
$E(B-V)_{\text{lines}}$ colour excess of the nebular lines light	0.0, 0.1, 0.2, 0.3, 0.4, 0.5, 0.6, 0.7, 0.8
Continuum attenuation $E(B-V)_{\text{stellar}}$ fraction relative to $E(B-V)_{\text{lines}}$	0.44
Ratio of total to selective extinction $A_V/E(B-V)$	3.1
Extinction law	Cardelli et al. (1989)
Redshift values	0.01–0.40 (step 0.01)
Number of models per redshift	194 400

Appendix B: Catalogue description

Table B.1. Catalogue keywords for the JOLINES catalogue. All emission line fluxes are provided in units of 10^{-15} erg s $^{-1}$ cm $^{-2}$.

Keyword	Description
TILE_ID	Tile ID of the reference r band (miniJPAS and J-NEP) or i band (J-PAS EDR)
NUMBER	Number id assigned by SExtractor to the object in J-PAS.
R.A.	Right ascension (J2000)
Dec.	Declination (J2000)
PhotoZ	Spectrophotometric redshift
o2_3727	[O II] λ 3727 emission-line doublet flux
err_3727	[O II] λ 3727 emission-line doublet flux uncertainty
ew_3727	[O II] λ 3727 emission-line doublet equivalent width
ne3_3869	[Ne III] λ 3869 emission-line flux
err_3869	[Ne III] λ 3869 emission-line flux uncertainty
ew_3869	[Ne III] λ 3869 emission-line flux equivalent width
hg+o3_4352	H γ λ 4340 + [O III] λ 4363 emission-line flux of the blend
err_4352	H γ λ 4340 + [O III] λ 4363 emission-line flux uncertainty of the blend
ew_4352	H γ λ 4340 + [O III] λ 4363 emission-line equivalent width of the blend
hb_4861	H β λ 4861 emission-line flux
err_4861	H β λ 4861 emission-line flux uncertainty
ew_4861	H β λ 4861 emission-line equivalent width
o3_4959	[O III] λ 4959 emission-line flux
err_4959	[O III] λ 4959 emission-line flux uncertainty
o3_5007	[O III] λ 5007 emission-line flux
err_5007	[O III] λ 5007 emission-line flux uncertainty
ew_5007	[O III] λ 5007 emission-line equivalent width
hb+o3_4910	H β λ 4861 + [O III] λ 4959 emission-line flux of the blend
err_4910	H β λ 4861 + [O III] λ 4959 emission-line doublet flux uncertainty
o3_4983	[O III] λ 4959, 5007 emission-line doublet flux
err_4983	[O III] λ 4959, 5007 emission-line doublet flux uncertainty
o1_6300	[O I] λ 6300 emission-line flux
err_6300	[O I] λ 6300 emission-line flux uncertainty
ew_6300	[O I] λ 6300 emission-line equivalent width
ha_6563	H α λ 6563 emission-line flux of the line
err_6563	H α λ 6563 emission-line flux uncertainty of the line
ew_6563	H α λ 6563 emission-line equivalent width
n2_6548	[N II] λ 6548 emission-line flux of the line
err_6548	[N II] λ 6548 emission-line flux uncertainty of the line
n2_6583	[N II] λ 6583 emission-line flux of the line
err_6583	[N II] λ 6583 emission-line flux uncertainty of the line
ew_6583	[N II] λ 6583 emission-line equivalent width
n2+ha_6555	[N II] λ 6548 + H α λ 6563 emission-line flux of the blend
err_6555	[N II] λ 6548 + H α λ 6563 emission-line flux uncertainty of the blend
ha+n2_6565	H α λ 6563 + [N II] λ 6548, 6583 emission-line flux of the blend
err_6565	H α λ 6563 + [N II] λ 6548, 6583 emission-line flux uncertainty of the blend
ew_6565	H α λ 6563 + [N II] λ 6548, 6583 emission-line equivalent width of the blend
ha+n2_6573	H α λ 6563 + [N II] λ 6583 emission-line flux of the blend
err_6573	H α λ 6563 + [N II] λ 6583 emission-line flux uncertainty of the blend
s2_6724	[S II] λ 6716, 6731 emission-line doublet flux
err_6724	[S II] λ 6716, 6731 emission-line doublet flux uncertainty
ew_6724	[S II] λ 6716, 6731 emission-line doublet equivalent width
s3_9069	[S III] λ 9069 emission-line flux
err_9069	[S III] λ 9069 emission-line flux uncertainty
ew_9069	[S III] λ 9069 emission-line equivalent width
s3_9531	[S III] λ 9531 emission-line flux
err_9531	[S III] λ 9531 emission-line flux uncertainty
...	...

Appendix C: AGN population

In this section, we analyse synthetic J-PAS photospectra generated for the AGN population in the DESI Early Data Release (EDR) (DESI Collaboration et al. 2024). AGN were selected using the spectroscopic fluxes provided by the FastSpecFit value-added catalogue (Moustakas et al. 2023; Moustakas et al. in prep.), associated with the DESI EDR, and the classical AGN demarcation in the BPT diagram (Baldwin et al. 1981), based on the $[\text{O III}]\lambda 5007/\text{H}\beta$ and $[\text{N II}]\lambda 6583/\text{H}\alpha$ line ratios (Kewley et al. 2001).

Following the methodology described in Section 3.2, the synthetic AGN photospectra were processed by performing continuum fitting with CIGALE, subtracting the best-fit continuum, and extracting the fluxes of the brightest emission lines listed in Table 1. The recovered emission-line fluxes were then directly compared with the corresponding spectroscopic measurements in the FastSpecFit catalogue (Fig. C.1). The derived line fluxes for AGN show excellent agreement with the spectroscopic values, confirming that robust continuum subtraction via SED fitting, without including an explicit AGN component, can still be applied successfully to this population.

This is primarily due to the moderate or low contribution of AGN to the optical continuum in these objects (note that bright, point-like quasars are excluded from the sample; see the target selection in Section 2) and the flexibility of the extensive model grid (Table 2), which can accommodate potential AGN contamination in the continuum using stellar population templates. Moreover, the AGN templates available in CIGALE are primarily designed for modelling dust emission in the infrared and provide limited flexibility in the optical range, where the emission is typically represented by a single power-law. Therefore, including such models would not significantly enhance the continuum modelling in the optical regime.

This test confirms that our method for continuum subtraction and emission-line flux extraction can also be reliably applied to the AGN population, recovering line fluxes without introducing significant biases.

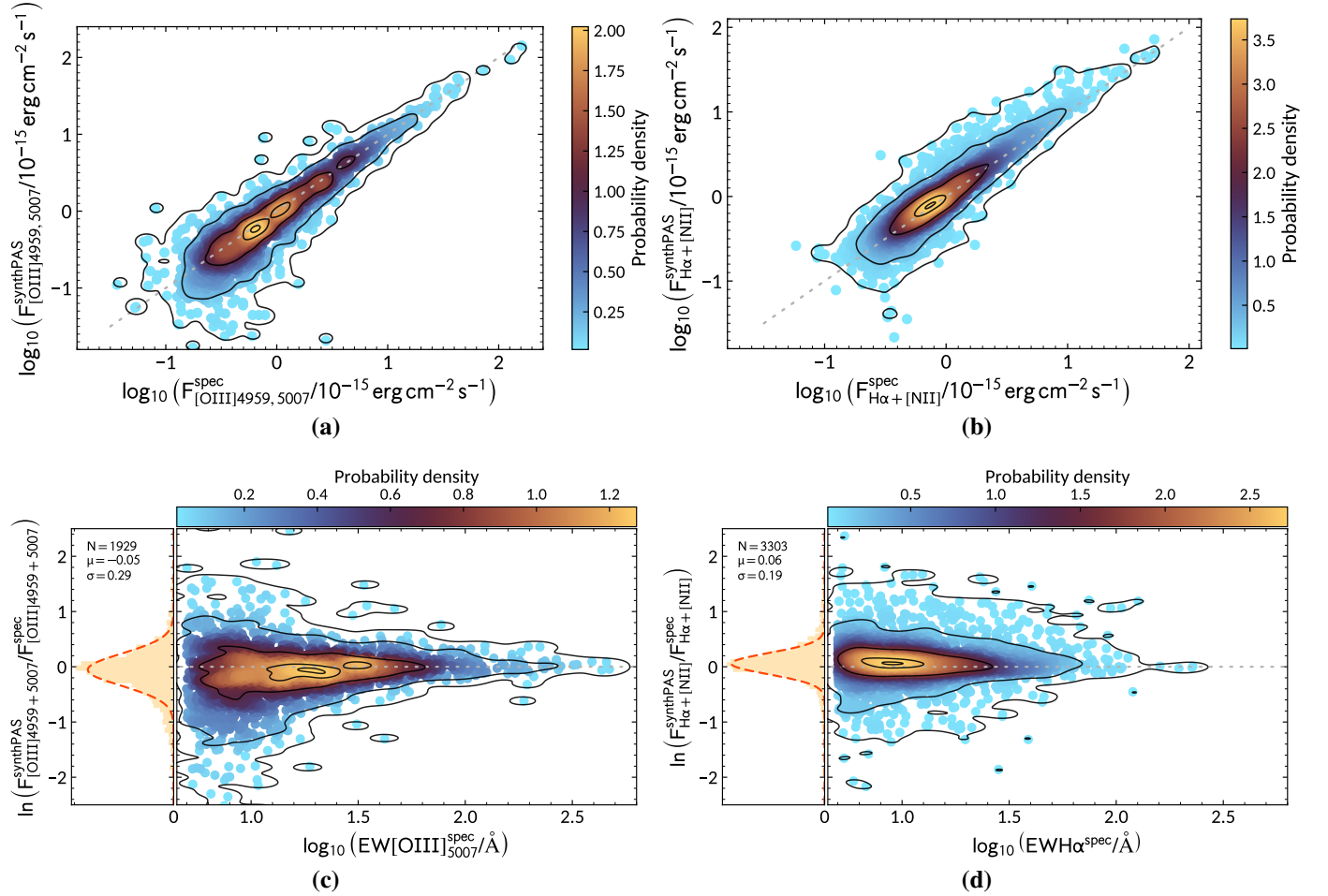


Fig. C.1. Same as Fig. 5, but for the AGN population in the DESI EDR.